generates a continuous red, green and blue digital record of the sediment core surface. A single composite record of colour intensity was compiled by sampling the continuous downcore profiles of red, green and blue colour intensity from the core drives at an increment of 0.5 mm. The three colour channels covary ($r^2 = 0.60$–0.99); we chose to use the red colour channel to document the downcore concentration of the laminae in the record because it exhibits slightly higher variance than either the blue or the green channel.

Data analysis

The age model for the new record is based on the same radiocarbon chronology used in ref. 4. The laminae dated by accelerator mass spectrometry ^{14}C of terrestrial microfossils in the record of ref. 4 are distinctive, and could be confidently identified in the new cores. By creating a composite section from overlapping drives, we were able to improve on the original age model. We adopted the constant carbon accumulation model (CCAM) and an event model (EM) to allocate time between dated intervals[4,8]. The CCAM assumes that the rate of organic carbon deposition has remained nearly constant between radiocarbon-dated intervals through the Holocene, and this continuous sedimentation was punctuated by nearly instantaneous clastic depositional events. The EM is based on the assumption that each of the clastic laminae was deposited during a single ENSO event with a temporal duration of 6 months, and we based this hypothesis on discharge data from the Rio Chira, which display high flow for a period of 6 months during an ENSO event[18]. Clastic events were identified in the colour intensity profile as peaks in colour intensity units that exceed the surrounding background laminae by 15 colour intensity units or more[8]. After time was assigned to the clastic laminae, the remaining time was distributed linearly between radiocarbon dates. One advantage of the EM over the CCAM is that it assigns equal magnitude to each of the events, thereby removing any effects that sediment compaction may have on the colour of the light-coloured laminae at the base of the record. Data archived at the NOAA Paleoclimatology Program and available online at: http://www.ngdc.noaa.gov/paleo/pubs/moy2002.

Received 15 May; accepted 8 October 2002; doi:10.1038/nature01194.

1. Thompson, L. G., Mosley-Thompson, E. & Thompson, P. A. *El Nino: Historical and Paleoclimate Aspects of the Southern Oscillation* (eds Diaz, H. F. & Markgraf, V.) 295–322 (Cambridge Univ. Press, Cambridge, 1992).
2. Cook, E. R., D'Arrigo, R. D., Cole, J. E., Stahle, D. W. & Villalba, R. *El Nino and the Southern Oscillation* (eds Diaz, H. F. & Markgraf, V.) 297–323 (Cambridge Univ. Press, Cambridge, 2000).
3. Tudhope, A. W. *et al.* Variability in the El Nino:Southern oscillation through a glacial–interglacial cycle. *Science* **291,** 1511–1517 (2001).
4. Rodbell, D. T. *et al.* An ~15,000-year record of El Nino-driven alluviation in southwestern Ecuador. *Science* **283,** 516–520 (1999).
5. Vuille, M., Bradley, R. S. & Keimig, F. Climate variability in the Andes of Ecuador and its relation to tropical Pacific and Atlantic sea surface temperature anomalies. *J. Clim.* **13,** 2520–2535 (2000).
6. Torrence, C. & Compo, G. P. A practical guide to wavelet analysis. *Bull. Am. Meteorol. Soc.* **79,** 61–78 (1998).
7. Gilman, D. L., Fuglister, F. J. & Mitchell, J. M. On the power spectrum of "red noise". *J. Atmos. Sci.* **20,** 182–184 (1963).
8. Moy, C. M. *A Continuous Record of Late-Quaternary El Nino-Southern Oscillation from the Southern Ecuadorian Andes* Thesis Syracuse Univ. (2000).
9. Hansen, B. C. S. *et al.* Late-glacial and Holocene vegetation history from two sites in the western cordillera of southern Ecuador. *Paleogeogr. Paleoclimatol. Paleoecol.* (in the press).
10. Rodbell, D. T. The timing of the last deglaciation in Cordillera Oriental, northern Peru, based on glacial geology and lake sedimentology. *Geol. Soc. Am. Bull.* **105,** 923–934 (1993).
11. Rodbell, D. T., Bagnato, S., Nebolini, J. C., Seltzer, G. O. & Abbott, M. B. A late glacial-Holocene tephrochronology for glacial lakes in southern Ecuador. *Quat. Res.* **57,** 343–354 (2002).
12. Cole, J. Paleoclimate: A slow dance for El Nino. *Science* **291,** 1496–1497 (2001).
13. Sandweiss, D. H. *et al.* Variation in Holocene El Nino frequencies: Climate records and cultural consequences in ancient Peru. *Geology* **29,** 603–606 (2001).
14. Clement, A. C., Seager, R. & Cane, M. A. Suppression of El Nino during the mid-Holocene by changes in the Earth's orbit. *Paleoceanography* **15,** 731–737 (2000).
15. Bond, G. C. *et al. Mechanisms of Global Change at Millennial Time Scales* Geophysical Monograph Series 112 (eds Clark, P.Webb, R. & Keigwin, L. D.) 35–58 (American Geophysical Union, Washington, DC, 1999).
16. Stuiver, M., Braziunas, T. F., Becker, B. & Kromer, B. Climatic, solar, oceanic, and geomagnetic influences on Late-Glacial and Holocene atmospheric $^{14}C/^{12}C$ change. *Quat. Res.* **35,** 1–24 (1991).
17. Clement, A. C. & Cane, M. A. *Mechanisms of Global Climate Change at Millennial Time Scales* Geophysical Monograph Series 112 (eds Clark, P. U., Webb, R. S. & Keigwin, L. D.) 363–371 (American Geophysical Union, Washington, D.C., 1999).
18. Martin, L. *et al.* Southern-Oscillation signal in South-American paleoclimatic data of the last 7000 years. *Quat. Res.* **39,** 338–346 (1993).

Acknowledgements We thank S. Bagnato and J. Turnbell for field assistance, and J. Lewalle for guidance with the wavelet analysis. Discussions with M. Cane, A. Clement and G. Compo significantly improved the manuscript. Funding was provided by the US NSF Earth System History Program (to G.O.S. and D.T.R.), and the Geological Society of America (GSA), the Quaternary Geology and Geomorphology Division of GSA, and the Syracuse University Department of Earth Sciences (to C.M.M).

Competing interests statement The authors declare that they have no competing financial interests.

Correspondence and requests for materials should be addressed to C.M.M. (e-mail: moyc@stanford.edu).

First-principles study of illite–smectite and implications for clay mineral systems

Lars Stixrude & Donald R. Peacor

Department of Geological Sciences, The University of Michigan, Ann Arbor, Michigan 48109, USA

Illite–smectite interstratified clay minerals are ubiquitous in sedimentary basins and they have been linked to the maturation, migration and trapping of hydrocarbons[1], rock cementation[2], evolution of porewater chemistry during diagenesis[3] and the development of pore pressure[4]. But, despite the importance of these clays, their structures are controversial. Two competing models exist, each with profoundly different consequences for the understanding of diagenetic processes: model A views such interstratified clays as a stacking of layers identical to endmember illite and smectite layers, implying discrete and independently formed units (fundamental particles)[5], whereas model B views the clays as composed of crystallites with a unique structure that maintains coherency over much greater distances, in line with local charge balance about interlayers[6]. Here we use first-principles density-functional theory to explore the energetics and structures of these two models for an illite–smectite interstratified clay mineral with a ratio of 1:1 and a Reichweite parameter of 1. We find that the total energy of model B is 2.3 kJ atom^{-1} mol^{-1} lower than that of model A, and that this energy difference can be traced to structural distortions in model A due to local charge imbalance. The greater stability of model B requires re-evaluation of the evolution of the smectite-to-illite sequence of clay minerals, including the nature of coexisting species, stability relations, growth mechanisms and the model of fundamental particles.

Illite and smectite both consist of aluminosilicate layers alternating with interlayers. In illite the charge of non-exchangeable interlayer cations is balanced by a greater net negative charge on the layers due largely to the substitution of Al for Si in the tetrahedral sheets. The mineral rectorite is the regularly interstratified sequence of illite- and smectite-like layers with a ratio of 1:1 and a Reichweite (R) ordering parameter R1. The illite- and smectite-like components of rectorite may be viewed as being centred either on the layers or on the interlayers (Fig. 1). The former view corresponds to model A: as in pure illite or smectite, the two tetrahedral sheets of each layer have the same composition; each interlayer is identical and is adjacent to a high-charge and a low-charge layer. In model B interstratification is viewed as being interlayer centred: each layer is identical and contains an Al-rich and an Al-poor tetrahedral sheet; up-down alternation of these layers results in two distinct interlayers, one adjacent to low-charge tetrahedral sheets and the other to high-charge tetrahedral sheets. Model B is consistent with alternating K-rich and K-poor interlayers, as implied by X-ray diffraction[7].

Small crystal sizes, complex composition, and turbostratic stacking (disordered rotations about the layer normal) in illite–smectite clays prevent complete experimental specification of the structure. However, advances in solid-state theory and computing power allow the exploration of even complex crystal structures such as clays. To evaluate the energetics of illite–smectite clays, and to test models A and B, we performed first-principles quantum mechanical calculations based on density-functional theory in the local density approximation. We considered the system $K_xAl_2(Al_xSi_{4-x})O_{10}(OH)_2$, where $x = 1$ (muscovite) and $x = 0$ (pyrophyllite) are endmembers of the illite–smectite series. We determined the total energies of fully

relaxed structures of models A and B for $x = 0.5$, which corresponds to a 1:1 R1 illite–smectite (I–S) composition (Fig. 1). For each model, the cell shape and internal atomic coordinates were systematically adjusted until the energy was minimized and the stress was hydrostatic. Energy minimization was performed at constant volume, which we assumed to be that of muscovite ($V = 943$ Å^3 per 82 atoms). All computations were performed with the plane-wave pseudopotential method using the Vienna Ab Initio Simulation Package (VASP)[8]. This method has been used successfully to study clays[9].

We find that model A has a total energy that is substantially higher than that of model B. The difference in energy (24 meV atom^{-1}, or 2.3 kJ atom^{-1} mol^{-1}) is comparable to the thermal energy at ambient temperature. For comparison, the quartz–cristobalite enthalpy difference at ambient conditions is more than a factor of two smaller (1 kJ atom^{-1} mol^{-1}) (ref. 10). The energy difference can be understood in terms of the two model structures: whereas in model B the excess charge of the interlayer K is balanced locally by charge-deficient tetrahedral sheets, in model A charge deficiency is disposed asymmetrically about the interlayer, allowing for only partial local balance of the interlayer charge.

The computations provide additional insight into the structural energetics of the two models. In model A, the asymmetric charge about the interlayer leads to a displacement of the K ion towards the charge-deficient layer by 0.7 Å. The proximity of the K ion causes substantial distortions of the coordination polyhedra, which contribute to the energetic instability of model A: the Al tetrahedron shows a variance of bond angles (units: degrees squared) (ref. 11) $\sigma = 46$, and three of the Si tetrahedra have $\sigma > 29$. In contrast, tetrahedra in model B show $2 < \sigma < 10$, within the range of values found experimentally in crystal-structure refinements of clays and micas (0.2–14.2) (ref. 12). As expected for dioctahedral phyllosilicates, OH bonds in both models are inclined towards the vacant site in the octahedral sheet, forming an angle (δ) with respect to the layer normal. In model B, the OH bonds about the K interlayer show $\delta = 69$–$75°$, in agreement with experimental measurements in muscovite[13,14]. In contrast, model A shows much larger inclinations: the OH bonds nearest to the K ion show $\delta = 97$–$99°$, that is, the hydrogen ions are forced below the plane of oxygen ions to which they are bonded.

The fact that differences in energy and structure between the two models can be understood in terms of local charge balance is important for the applicability of our results to natural illite–smectite. Layers of illite–smectite are known to stack in a variety of ways, including turbostratically. Different stacking sequences must result in small adjustments in local structure. However, such adjustments and the resultant differences in energy are trivial compared with the major differences between the tested models, and do not affect the conclusions of this study. In natural samples, the difference in charge between low- and high-charge elements is reduced as compared with our idealized structures based on end-members. Differences in energy and structure between models A and B are expected to be reduced proportionately, but to remain large to the extent that low-charge and high-charge elements remain distinct.

The structure of model B is significant because it shows that the energetically favourable state of R1 I–S is not a simple mixture of endmember layers of illite and smectite. The structural components of model B, including the 2:1 layers (tetrahedral–octahedral–tetrahedral, TOT), are not found in either endmember. This has important implications for the thermodynamic properties of illite–smectite clays. Because these are difficult to obtain experimentally at low temperatures of formation, there have been many previous attempts to model thermodynamic properties[15]. These models did not consider the unique low-energy ordered state of R1 I–S represented by model B. The difference in energy between model B and a nanoscale mechanical mixture of illite and smectite layers (model A) is substantial and must be considered in future modelling of thermodynamic properties.

The unique structure of R1 I–S shows that it is a relatively stable phase of low potential energy, as demonstrated also for smectite and illite by their common occurrence. Our results imply that the

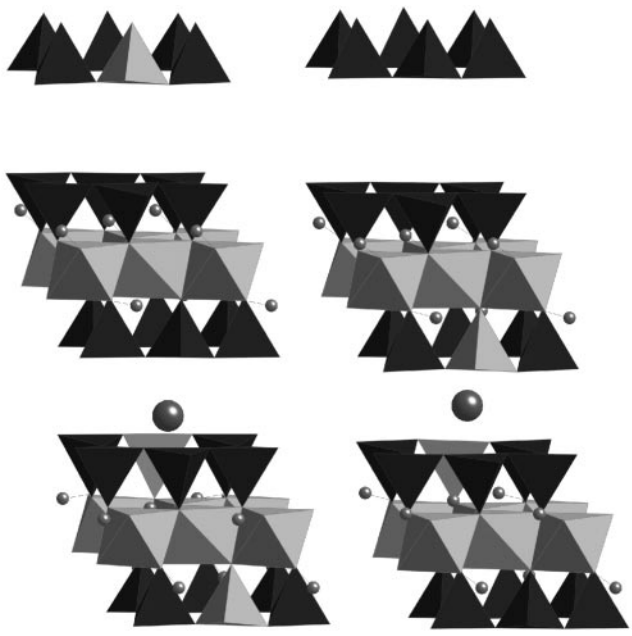

Figure 1 Fully relaxed computed structures of model A (left) and model B (right) 1:1 illite–smectite. Dark tetrahedra, Si; light tetrahedra, Al; large dark spheres, K; small dark spheres, H. Al octahedra are also shown. The repeat unit in the *c*-direction in each case contains one occupied and one unoccupied interlayer. For all calculations, we assumed an energy cut-off of 500 eV and a $2 \times 2 \times 2$ Monkhorst–Pack[29] *k*-point mesh. Computed lattice parameters for model A: $a = 5.168$, $b = 8.947$, $c = 20.808$ Å, $\alpha = 89.97°$, $\beta = 101.40°$, $\gamma = 89.96°$; and model B: $a = 5.130$, $b = 8.868$, $c = 21.163$ Å, $\alpha = 89.82°$, $\beta = 101.61°$, $\gamma = 89.96°$, are within 2% of those measured for a natural K-rich rectorite without interlayer water[30].

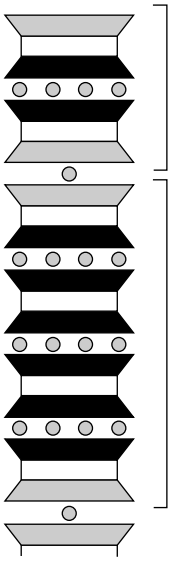

Figure 2 Schematic of illite-rich illite–smectite structure showing interlayer cations (spheres) and 2:1 layers. Shading of the tetrahedral sheets indicates relative concentration of tetrahedral Al, with the darkest shading corresponding to the highest concentrations (greatest charge deficiency). Two illite-like units, bounded by cleavage planes, one 20-Å thick and one 40-Å thick, are indicated by the brackets.

commonly observed assemblages in the illite–smectite series should be pure smectite, smectite + R1 I–S, pure R1 I–S, R1 I–S + illite, and illite. The series is not continuous, but it has gaps between smectite and R1 I–S, and between illite-rich illite–smectite and illite, such gaps being analogous to immiscibility gaps. Indeed, recent transmission electron microscope (TEM) studies[16] demonstrated the occurrence of these assemblages. TEM data show a large gap between smectite and R1 I–S, and a smaller gap between a range of illite-rich illite–smectite and illite. Figure 2 shows the structure relations for illite-rich illite–smectite. The Al–Si ordering implied by our model verifies that it can be viewed as interstratified packets of illite and R1 I–S (ref. 17), not illite and smectite layers. This does not mean that complete sequences of randomly ordered smectite-like and illite-like layers cannot occur. Such interstratified clays may form where crystallization favours extreme disorder. Our results do imply, however, that much if not most of 'mixed-layered illite–smectite' involves phases for which ordered R1 I–S is the critical, unique phase, analogous to corrensite in the chlorite–smectite (saponite) system[18].

This model at first appears incompatible with X-ray diffraction (XRD) data, which are consistent with a continuous series of interstratified illite–smectite (ref. 19) as expressed in Reichweite nomenclature[20], and which provides support to fundamental particle theory[5]. We tentatively suggest that the differences in interpretations of XRD patterns and TEM observations are caused by differences in sample preparation. TEM analysis involves ion-milled samples that retain their original texture, whereas XRD analysis generally involves mechanical and chemical treatment that causes separation of layers, especially along low-charge interlayers, which are reconstituted in altered sequences in samples for which interparticle diffraction determines characteristics of XRD patterns[21].

Fundamental particle theory[5] requires that illite–smectite comprise illite and smectite layers and is thus incompatible with the results of this study. The theory assumes that R1 I–S comprises independent elementary particles of illite (20-Å-thick units centred on an illite interlayer) and smectite (10-Å-thick elementary smectite particles). Illite-rich illite–smectite is modelled as equivalent to independent fundamental particles comprising coherently related illite layers. Interfaces between particles in aggregates are modelled as being smectite-like and, through interparticle X-ray diffraction, as giving rise to sequences that behave like illite–smectite (ref. 21). Fundamental particles are theorized to exist not only in samples prepared for XRD, but also in original geologic samples. This model has been criticized[22] on the basis of TEM observations of intact samples. Our results show that the 2:1 layers in a sequence of illite-rich illite–smectite are not independent (Fig. 2). The relative proportions of Al and Si in any one layer are directly related to those in adjacent layers. Moreover, such layer sequences are compatible with the data for thickness of separates on which the fundamental particle theory is based[5]. Cleavage across low-charge interlayers must produce separate illite-like particles (Fig. 2), but with interfaces that are truly low charge (Al-poor tetrahedral sheets), consistent with observed relations[6,23] and inconsistent with the smectite-like behaviour attributed to fundamental particles. We suggest, therefore, that fundamental particle theory is based on an invalid crystal-chemical model and incorrectly implies equality of states of clay separates and crystallites in unprocessed rocks.

Several mechanisms for the formation of illite–smectite during diagenesis of pelitic sediments have been proposed, but they can be approximated as two types, layer-by-layer replacement and dissolution/neocrystallization[24]. Our results favour dissolution and neocrystallization[25,26] because the differences in Al–Si ordering between rectorite and illite or smectite are incompatible with transformations by means of solid-state diffusion of Al and Si at the low transformation temperatures observed in Nature[25]. Previous work, based on XRD patterns, has indicated layer-by-layer replacement of smectite by illite, for example in Gulf Coast mudstones, which show a continuous series of mixed-layered illite–smectite with increasing depth by XRD[27]. The layer-by-layer mechanism, however, is incompatible with the presence of discrete phases separated by gaps.

The validity of theories of crystal growth is based on observations of the sizes and shapes of crystals in evolving systems. The most recent theories of growth of illite–smectite have been tested assuming that particle thicknesses (as measured in separates by XRD) are fundamental particles; that is, they consist only of the sequences of illite layers obtained in separates[28]. As shown in Fig. 2, however, layers that are separated by a low-charge interlayer (smectite-like) are not independent, and thus a layer added during growth is not a randomly determined illite or smectite layer. Adjacent layers have structures that are mutually dependent, as is true of any crystal structure and defined in the case of illite–smectite by the distribution of Al in the tetrahedral sheets. We view the common lack of coherency (turbostratic stacking) that occurs across low-charge interlayers as a defect in a continuous crystal, albeit a defect that is the rule rather than the exception; that is, packets of layers are analogous to McEwan crystallites[6]. No theory of crystal growth can be applied successfully to measures of crystal size that are not equivalent to actual growth units. The kinds of complete layer sequences shown in Fig. 2 are inferred to represent growth units, in contrast to units consisting only of the illite-like components in separates as interpreted by fundamental particle theory. We consider that determinations of growth mechanisms in natural systems that assume the existence of fundamental particles in clay separates are therefore in error. □

Received 21 May; accepted 19 September 2002; doi:10.1038/nature01155.

1. Weaver, C. E. Possible uses of clay minerals in search for oil. *Bull. Am. Assoc. Petrol. Geol.* **44,** 1505–1518 (1960).
2. Boles, J. R. & Franks, S. G. Clay diagenesis in Wilcox sandstones of southwest Texas—implications of smectite diagenesis on sandstone cementation. *J. Sedim. Petrol.* **49,** 55–70 (1979).
3. Brown, K. M., Saffer, D. M. & Bekins, B. A. Smectite diagenesis, pore-water freshening, and fluid flow at the toe of the Nankai wedge. *Earth Planet. Sci. Lett.* **194,** 97–109 (2001).
4. Bethke, C. M. Inverse hydrologic analysis of the distribution and origin of Gulf Coast-type geopressured zones. *J. Geophys. Res.* **91,** 6535–6545 (1986).
5. Nadeau, P. H., Wilson, M. J., McHardy, W. J. & Tait, J. M. Interstratified clays as fundamental particles. *Science* **255,** 923–925 (1984).
6. Altaner, S. P., Weiss, C. A. & Kirkpatrick, R. J. Evidence from ^{29}Si NMR for the structure of mixed layer illite–smectite clay minerals. *Nature* **331,** 699–702 (1988).
7. Brown, G. Crystal-structures of clay-minerals and related phyllosilicates. *Phil. Trans. R. Soc. Lond. A* **311,** 221–240 (1984).
8. Kresse, G. & Furthmüller, J. Efficient iterative schemes for ab initio total-energy calculations using a plane-wave basis set. *Phys. Rev. B* **54,** 11169–11186 (1996).
9. Stixrude, L. Talc under tension and compression: spinodal instability and structure at high pressure. *J. Geophys. Res.* (in the press).
10. Berman, R. G. Internally-consistent thermodynamic data for minerals in the system Na_2O-K_2O-CaO-MgO-FeO-Fe_2O_3-Al_2O_3-SiO_2-TiO_2-H_2O-CO_2. *J. Petrol.* **29,** 445–522 (1988).
11. Robinson, K., Gibbs, G. V. & Ribbe, P. H. Quadratic elongation—quantitative measure of distortion in coordination polyhedra. *Science* **172,** 567–570 (1971).
12. Smyth, J. R. & Bish, D. L. *Crystal Structures and Cation Sites of the Rock-Forming Minerals* (Allen and Unwin, Boston, 1988).
13. Rothbauer, R. Untersuchung eines 2M1-Muskovits mit Neutronenstrahlen. *Neues Jb. Mineral. Mh.* **4,** 143–154 (1971).
14. Rossman, G. R. Spectroscopy of micas. *Rev. Mineral.* **13,** 145–181 (1984).
15. Essene, E. J. & Peacor, D. R. Clay mineral thermometry—A critical perspective. *Clays Clay Minerals* **43,** 540–553 (1995).
16. Dong, H., Peacor, D. R. & Freed, R. L. Phase relations among smectite, R1 illite-smectite, and illite. *Am. Mineral.* **82,** 379–391 (1997).
17. Schroeder, P. A. & Irby, R. Detailed X-ray diffraction characterization of illite-smectite from an Ordovician K-bentonite, Walker County, Georgia, USA. *Clay Minerals* **33,** 671–674 (1998).
18. Shau, Y. H., Peacor, D. R. & Essene, E. J. Corrensite and mixed-layer chlorite/corrensite in metabasalt from northern Taiwan: TEM/AEM, EMPA, XRD, and optical studies. *Contrib. Mineral. Petrol.* **105,** 123–142 (1990).
19. Srodon, J., Morgan, D. J., Eslinger, E. V., Eberl, D. D. & Karlinger, M. A. Chemistry of illite/smectite and end-member illite. *Clays Clay Minerals* **34,** 368–378 (1986).
20. Srodon, J. Nature of mixed-layer clays and mechanisms of their formation and alteration. *Annu. Rev. Earth Planet. Sci.* **27,** 19–53 (1999).
21. Nadeau, P. H., Wilson, M. J., McHardy, W. J. & Tait, J. M. Interparticle diffraction: a new concept for interstratified clays. *Clay Minerals* **19,** 757–769 (1984).
22. Kasama, T., Murakami, T., Kohyama, N. & Watanabe, T. Experimental mixtures of smectite and rectorite: Re-investigation of "fundamental particles" and "interparticle diffraction". *Am. Mineral.* **86,** 105–114 (2001).
23. Jakobsen, H. J., Nielsen, N. C. & Lindgreen, H. Sequences of charged sheets in rectorite. *Am. Mineral.* **80,** 247–252 (1995).

24. Altaner, S. P. & Ylagan, R. F. Comparison of structural models of mixed-layer illite-smectite and reaction mechanisms of smectite illitization. *Clays Clay Minerals* **45,** 517–533 (1997).
25. Ahn, J. H. & Peacor, D. R. A transmission and analytical electron microscopic study of the smectite to illite transition. *Clays Clay Minerals* **34,** 165–179 (1986).
26. Nadeau, P. H., Wilson, M. J., McHardy, W. J. & Tait, J. M. The conversion of smectite to illite during diagenesis: evidence from some illitic clays from bentonites and sandstones. *Mineral. Mag.* **49,** 393–400 (1985).
27. Hower, J., Eslinger, E. V., Hower, M. E. & Perry, E. A. Mechanism of burial metamorphism of argillaceous sediments: Mineralogical and chemical evidence. *Geol. Soc. Am. Bull.* **87,** 725–737 (1976).
28. Eberl, D. D., Drits, V. A. & Srodon, J. Deducing growth mechanisms for minerals from the shapes of crystal size distributions. *Am. J. Sci.* **298,** 499–533 (1998).
29. Monkhorst, H. J. & Pack, J. D. Special points for Brillouin-zone integrations. *Phys. Rev. B* **13,** 5188–5192 (1976).
30. Benincasa, E., Brigatti, M. F., Medici, L. & Poppi, L. K-rich rectorite from kaolinized micaschist of the Sesia-Lanzo Zone, Italy. *Clay Minerals* **36,** 421–433 (2001).

Acknowledgements This work was supported by the US National Science Foundation.

Competing interests statement The authors declare that they have no competing financial interests.

Correspondence and requests for materials should be addressed to L.S. (e-mail: stixrude@umich.edu).

Synchronization of animal population dynamics by large-scale climate

Eric Post* & Mads C. Forchhammer†

** Department of Biology, The Pennsylvania State University, 208 Mueller Lab, University Park, Pennsylvania 16802, USA*
† Department of Population Ecology, Zoological Institute, University of Copenhagen, Universitetsparken 15, DK-2100 Copenhagen, Denmark

The hypothesis that animal population dynamics may be synchronized by climate[1] is highly relevant in the context of climate change because it suggests that several populations might respond simultaneously to climatic trends if their dynamics are entrained by environmental correlation. The dynamics of many species throughout the Northern Hemisphere are influenced by a single large-scale climate system, the North Atlantic Oscillation (NAO)[2,3], which exerts highly correlated regional effects on local weather[4]. But efforts to attribute synchronous fluctuations of contiguous populations to large-scale climate are confounded by the synchronizing influences of dispersal or trophic interactions[5]. Here we report that the dynamics of caribou and musk oxen on opposite coasts of Greenland show spatial synchrony among populations of both species that correlates with the NAO index. Our analysis shows that the NAO has an influence in the high degree of cross-species synchrony between pairs of caribou and musk oxen populations separated by a minimum of 1,000 km of inland ice. The vast distances, and complete physical and ecological separation of these species, rule out spatial coupling by dispersal or interaction. These results indicate that animal populations of different species may respond synchronously to global climate change over large regions.

Despite widespread evidence that several species' populations respond to large-scale climatic fluctuation[2,3], attributing spatial synchrony in animal population dynamics to environmental forcing is problematic[6]. The correlated dynamics of populations of Soay sheep (*Ovis aries*) on separate islands[7] is strongly indicative of spatial coupling by climate, as is the segregation of the structural dynamics of Canada lynx (*Lynx canadensis*) populations into regions experiencing similar climatic regimes[8]. But the high degree of gene flow among the lynx populations indicates that there is also a high degree of dispersal among them[9]. The pervasive influence of the NAO[10] in the population dynamics of vertebrates throughout the Northern Hemisphere[2,8,11–13], including Soay sheep[13–15] and Canada lynx[8], suggests that the NAO has the potential to contribute to spatial synchrony across broad geographic scales in these and other populations[16]. The challenge therefore lies in identifying systems in which the climatic signal in population synchrony is not obscured by dispersal or trophic interactions.

We have analysed continental-scale data on the long-term dynamics of caribou (*Rangifer tarandus*) and musk oxen (*Ovibos moschatus*) in Greenland, where a continent-wide ice sheet separates the two species physically and ecologically (ref. 17 and Fig. 1a). Caribou are indigenous to west Greenland but do not inhabit northeast Greenland, where musk oxen are indigenous (Fig. 1a). Although time series data on population dynamics exist for seven caribou and six musk oxen populations in Greenland, our analysis focuses primarily on six caribou and five musk oxen populations whose dynamics are influenced by the NAO (Methods). The physical isolation of these two species, coupled with their lack of interspecific competition for food or shared predators in Greenland, greatly simplifies the analysis of climate-induced synchrony. In addition, evidence indicates that the dynamics of populations of

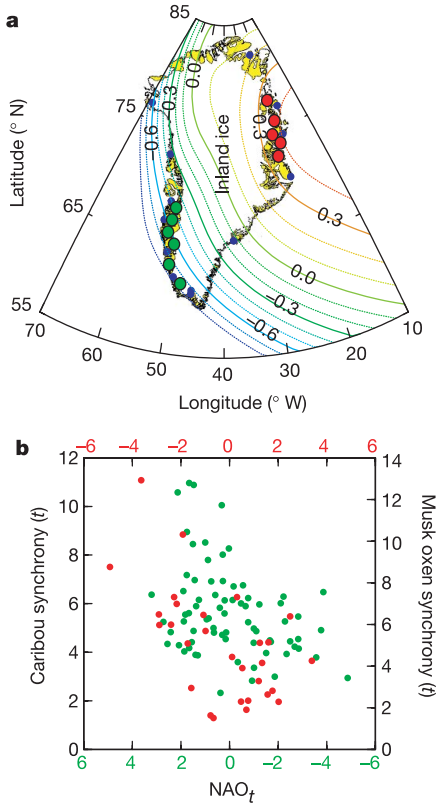

Figure 1 Correlations between the NAO and local weather and population synchrony in Greenland. **a**, Spatial gradient in the correlation between local winter temperature and the winter NAO index across Greenland. Contours (interval 0.1) denote correlations between the NAO winter index and average winter (December to March) temperature from 12 weather stations (blue dots) over the period 1967 to 1995. Correlative contours were constructed as described[29] using linear interpolation[30]. Red and green circles show the location of the respective musk oxen and caribou populations used in our analyses. **b**, Correlations between the winter NAO index and synchrony (Methods) across populations of musk oxen (red; $R^2 = 0.45$, $P < 0.001$) and caribou (green; $R^2 = 0.43$, $P < 0.001$) in northeast and west Greenland, respectively. Inclusion of the two populations that are not influenced by the NAO resulted in poorer correlations for both species (Methods). The top *x*-axis applies to the correlation with musk oxen synchrony, the bottom *x*-axis applies to the correlation with caribou synchrony; axes are reversed to show the same gradient from cold (left) to warm (right).

